Journal of Computational Physics **173,** 364–390 (2001)
doi:10.1006/jcph.2001.6883, available online at http://www.idealibrary.com on IDEAL®

Spectral Methods for Mesoscopic Models of Pattern Formation

David J. Horntrop,* Markos A. Katsoulakis,† and Dionisios G. Vlachos‡

*Department of Mathematical Sciences, New Jersey Institute of Technology, Newark, New Jersey 07102; †Department of Mathematics and Statistics, University of Massachusetts, Amherst, Massachusetts 01003; and ‡Department of Chemical Engineering, University of Delaware, Newark, Delaware 19716
E-mail: horntrop@njit.edu

Received October 2, 2000; revised July 2, 2001

In this paper we present spectral algorithms for the solution of mesoscopic equations describing a broad class of pattern formation mechanisms, focusing on a prototypical system of surface processes. These models are in principle stochastic integrodifferential equations and are derived directly from microscopic lattice models, containing detailed information on particle–particle interactions and particle dynamics. The enhanced computational efficiency and accuracy of spectral methods versus finite difference methods are also described.

Key Words: spectral methods; mesoscopic models; Monte Carlo; interacting particle systems.

1. INTRODUCTION

Intermolecular forces dictate macroscopic properties of matter and are inherently related to pattern formation in a number of phenomena exhibiting microphase separation, notably polymer blends, alloys, catalysis, epitaxial growth of advanced materials, and biology. Exact dynamic and equilibrium descriptions of these phenomena can be obtained by molecular simulations, such as molecular dynamics and Monte Carlo algorithms, for a given intermolecular potential [1]. Despite their widespread use, these computational methods are currently limited to short length and time scales, whereas morphological features seen in experiments or device sizes often invoke much larger space and/or time length scales [2]. This disparity underscores the need to develop theories for larger scales [3], which take into consideration microscopic details rather than relying only on phenomenology.

Recently, coarse-grained models of the master equation of Ising systems were developed, when the Hamiltonian describes spin exchange, spin flip, or a combination of the two mechanisms [4–9]. Such theories have been termed mesoscopic and local mean field. Through homogenization and asymptotics, the underlying macroscopic laws of interface velocity,

0021-9991/01 $35.00

surface tension, mobility, and critical nucleus size have also been derived [6, 11–13] and shown to have a direct dependence on the interaction potential. Thus for the first time, a direct rigorous analytical link of molecular interactions with macroscopic laws of transport and thermodynamics has been established. This link obviously enables comparison of experimentally measurable quantities to intermolecular forces as well as very efficient evaluation of different interaction potentials.

The mesoscopic equations studied here are derived from first principles, i.e., from a corresponding master equation describing the relevant microscopic processes, by a rigorous coarse graining. An important feature of mesoscopic theories is that they are exact in the limit that the interaction potential range becomes infinite without involving truncations or gradient expansions, which is in contrast to the Cahn–Hilliard [14] (or Cahn–Hilliard–Cook) and Allen–Cahn equations often employed to study phase separation of polymers [15–17]. While the issue of an infinite range potential may appear to be too restrictive, a first comparison of results from the mesoscopic theory with gradient Monte Carlo simulations under far from equilibrium conditions indicates that only a relatively short-range potential is adequate for quantitative agreement [9]. Moreover, asymptotics indicates that the deviation of the solution of the mesoscopic theory from the infinite-range potential decays in an exponential way, due to an underlying Large Deviation Principle, and decreases with the square root of the problem dimensionality; as a result, mesoscopic theories for 2D and 3D lattices require even shorter range interaction potentials [18]. Furthermore, underresolved small-scale fluctuations and finite-range interaction effects can be systematically incorporated in the mesoscopic models as stochastic corrections [9]. While further comparisons of Monte Carlo and mesoscopic simulations are needed, the agreement observed thus far is extremely encouraging and indicates that it may be possible to eventually replace intensive molecular simulations with relatively inexpensive solvers of mesoscopic partial differential equations (PDEs) for a large class of problems.

A major advantage of mesoscopic theories is their versatility. In particular, they can employ various interaction potentials including combinations of attractive and repulsive forces as well as anisotropic ones. Furthermore, various microscopic dynamics of diffusion can be studied (e.g., Metropolis, Kawasaki, Arrhenius, etc.) and various microscopic processes (e.g., diffusion coupled with adsorption, desorption, and reaction) can be exploited systematically. For instance, mesoscopic theories can be applied to systems ranging from nanoscale patterns in surface reaction adlayers on catalyst surfaces, to sintering of alloys, to diffusion on crystal surfaces and through membranes [9, 19, 20]. Due to the fundamental processes described by such theories (e.g., adsorption, desorption, reaction, and diffusion), extension from model systems to realistic situations and application of mesoscopic theory to additional research areas could be expected.

From the mathematical and numerical points of view, mesoscopic equations are stochastic integrodifferential PDEs that describe processes of different time scales. Furthermore, several phenomena, such as dynamics near bifurcation points and pattern evolution at late stages and ripening, exhibit long relaxation times that often preclude simulations from reaching equilibrium or steady state. This problem makes comparison with experiments difficult. In addition, parametric studies and on-line control of mesoscale patterns demand numerous such simulations, so computational cost becomes a crucial aspect in the success of mesoscopic theories. One objective of this work is to exploit the application of spectral methods to solving mesoscopic equations. Such methods are expected to efficiently and accurately solve mesoscopic theories with or without noise. Problems involving

long-range potentials such as electrostatics in ionic systems are expected to be solvable with unprecedented efficiency since longer range potentials do not require any additional computational effort for spectral methods. Furthermore, spectral methods can easily incorporate anisotropic potentials, nonlocal mobility terms, as well as convection–diffusion terms. In fact, the convection–diffusion terms can even be treated exactly in many instances through the use of appropriate integrating factors. A complete discussion of the advantages of the spectral methods in comparison to finite difference schemes, which have usually been employed until now in computational studies of mesoscopic models, is presented in subsequent sections of this paper. Extensions of the methods presented in this paper on stochastic mesoscopic equations will be presented in a follow-up publication.

The organization of this paper is as follows. In Section 2 we review mesoscopic theories for surface processes. The derivation of mesoscopic models from microscopics as well as the quantitative relation of microscopic and mesoscopic models to Ginzburg–Landau theories, at least for attractive microscopic interactions, are discussed in Appendices A and B, respectively. Numerical methods are discussed in Section 3, along with efficiency and accuracy issues in a comparison of spectral techniques with finite difference methods. In Section 4, scaling laws and asymptotic regimes are compared with numerical solutions. Finally, Section 5 summarizes the paper.

2. MESOSCOPIC MODELS FOR SURFACE PROCESSES

While mesoscopic models such as the ones described here can appear in a number of applications, in this paper we focus on processes occurring at fluid–solid interfaces such as in catalysis, adhesive surfaces, and biological cells. Surface processes have traditionally been modeled using continuum-type diffusion–reaction models [21], where the adsorptive layer has been assumed to be spatially uniform (global mean field theory). This approach either neglects particle interactions or treats them phenomenologically, while nonequilibrium statistical mechanics theories provide an exact microscopic description; see for instance [23] and [24]. The mathematical tools employed in the statistical mechanics models are interacting particle systems (IPS), which are Markov processes set on a lattice such as the Ising-type systems [25] describing the evolution of an order parameter at each lattice site. In this section we review mesoscopic evolution equations arising in surface processes and refer to Appendix A for a discussion on their derivation from corresponding microscopic stochastic mechanisms.

2A. Adsorption/Desorption

The first mechanism we discuss is the desorption of microscopic particles from a surface to the gas phase above and conversely the adsorption of a particle from the gas phase to the surface as shown schematically in Fig. 1. At a microscopic level this process is described by a spin flip in the order parameter; 1 is converted to 0 and vice versa under suitable microscopic dynamics such as Metropolis-type and Arrhenius (see Appendix A). For the former, the statistically averaged coverage u solves in a suitable asymptotic limit the mesoscopic equation

$$u_t = \psi(-\beta(J * u + h))[1 - u - \exp(-\beta h)u \exp(-\beta J * u)], \tag{2.1}$$

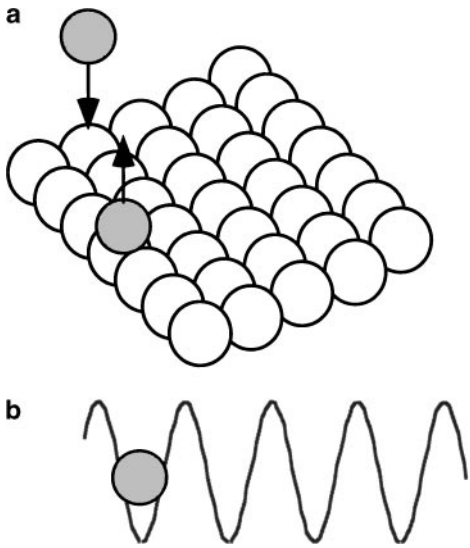

FIG. 1. (a) Schematic of surface atoms of a crystal (open spheres) and microscopic processes: Adsorption (A) of an atom (dotted sphere) from the fluid phase, desorption (D) of the adsorbate back to the fluid, and migration (M) of adsorbate along the surface. (b) One-dimensional cut of the potential energy surface describing species–crystal interactions in the limit of zero concentration ($J_m = J_d = 0$). Species diffuse from minima of the potential energy to adjacent sites by overcoming an energy barrier known as activation energy.

where ψ is associated with the microscopic spin flip rates, J is the interaction potential, u is a coarse-grained variable that can be viewed as the probability density of the coverage, β is the inverse temperature, and h denotes the external field. Similarly, for the Arrhenius adsorption/desorption dynamics, we have the mesoscopic equation

$$u_t = c_0[1 - u - \exp(-\beta h)u \exp(-\beta J * u)], \tag{2.2}$$

where c_0 is a rate constant.

Next we review some basic properties of (2.1) and (2.2). First, both equations are equipped with a comparison principle, at least when $J \geq 0$. Steady state solutions of either equation satisfy the algebraic equation

$$f(x) := \alpha(1 - x) - xe^{-\lambda x} = 0, \tag{2.3}$$

where $\alpha = \exp(\beta h)$ and $\lambda = J_0\beta$, $J_0 = \int J(r)\, dr$. Figure 2 shows schematically the phase diagram as a function of the external field α, and the interaction parameter λ. Outside the cuspy envelope, intermolecular forces are either weak or very strong resulting in a single-valued isotherm corresponding to the single root of (2.3). Region I corresponds to a dilute phase, Region III to a dense phase. Within the cuspy envelope (Region II), both phases may exist. In this case (2.3) has three solutions, $m_- = m_-(\alpha, \lambda) < m_0 = m_0(\alpha, \lambda) < m_+ = m_+(\alpha, \lambda)$, where m_+ and m_- correspond to the dense and the dilute phases of the system, respectively. The dynamics of cluster growth within Region II depends on the relative parameter location with respect to the *stationary coexistence* curve (the dotted line in Fig. 2), given by $\alpha = e^{-\lambda/2}$. In this last case the roots of (2.3) become $m_0 = \frac{1}{2}$ and $m_\pm = \frac{1}{2} \pm \nu$, for some $0 < \nu < \frac{1}{2}$.

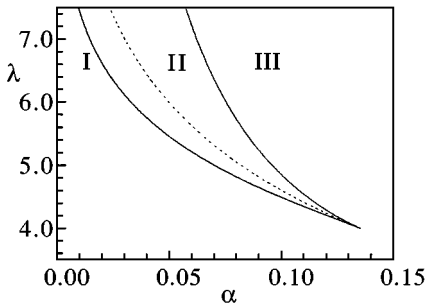

FIG. 2. Phase diagram for the system in (2.1) and (2.2). Within the cusp (Region II), the system is bistable and thus may have regions that are dilute while other regions are dense; outside this cusp, the system tends to be either dilute or dense. The line of stationary coexistence is the dotted line within Region II.

Standing and travelling waves for (2.1) and (2.2) play an important role in the long space/time asymptotics of mesoscopic equations [6, 13], since they connect high and low density phases, across a cluster boundary. The rigorous existence, uniqueness, and stability of such solutions follows from the analysis in [34], which covers a broad class of integrodifferential equations that admit a comparison principle. Other related works include [35, 36]. Note that for even potentials which are not necessarily radial we obtain direction-dependent standing and travelling waves [6].

2B. Surface Diffusion

The second mechanism we discuss is the diffusion of particles on a surface, as shown in Fig. 1. At the microscopic level this process is described by a spin exchange between the neighboring sites x and y, i.e., a spontaneous exchange of the values of the order parameter at x and y. The microscopic dynamics dictate the rates of the spin exchange, and typical examples are the Metropolis-type and Arrhenius dynamics. The mesoscopic model for Metropolis-type dynamics is [8]

$$u_t - D\nabla \cdot [\nabla u - \beta u(1-u)\nabla J * u] = 0, \tag{2.4}$$

where $D = \psi(0)$ and ψ is again associated to the spin exchange rates. For the Arrhenius diffusion mechanism we obtain the mesoscopic equation [9]

$$u_t - D\nabla \cdot \{\exp(-\beta J * u)[\nabla u - \beta u(1-u)\nabla J * u]\} = 0, \tag{2.5}$$

where $D = \exp(-\beta U_0)$. In both equations we assumed a zero external field h. If there is a nontrivial external field, then by introducing the free energy

$$E[u] = -\frac{1}{2}\int\int J(r-r')u(r)u(r')\,dr\,dr' + \int \frac{1}{\beta}[u\ln u + (1-u)\ln(1-u)]\,dr, \tag{2.6}$$

(2.4) and (2.5) can both be written as the constrained gradient flow

$$u_t - \nabla \cdot \left\{\mu[u]\nabla\left(\frac{\delta E[u]}{\delta u} + h\right)\right\} = 0. \tag{2.7}$$

In the case of (2.4) the mobility term $\mu[u]$ is $\mu[u] = D\beta u(1-u)$, while in the Arrhenius case (2.5) it is a nonlocal function given by $\mu[u]D\beta u(1-u)\exp(-\beta J * u)$. Note that in both equations the coverage u satisfies $0 \le u \le 1$ due to the presence of the term $u(1-u)$ in the mobilities, which enforces the exclusion principle (i.e., at most one particle per lattice site) and consequently the monolayer structure at the mesoscopic level.

Equations (2.4) and (2.5) include two competing forces: a Fickian diffusion term which competes with an uphill diffusion due to the attractive potnetial $J \ge 0$. We expect that when the parameter β is large, the particles will tend to organize in clusters, overcoming the Fickian diffusive effects. These heuristics become clearer with the use of a linearization argument around a constant coverage u_0, which yields a regime of *spinodal decomposition*. Indeed, we consider a solution $u = u_0 + \epsilon \exp(\omega t + i\xi \cdot x)$ of (2.4), for instance, where u_0 is a constant state and $\epsilon \ll 1$. The linearization of the equation around u_0 yields the dispersion relation

$$\omega = -|\xi|^2[1 - \beta u_0(1-u_0)\hat{J}(\xi)], \tag{2.8}$$

where $J_0 = \int J(r)\,dr$ and $\hat{J}$ denotes the Fourier transform of J. For example, the Fourier transform of the potential used as our example in this paper, $J(r) = (1/\sqrt{2\pi r_0^2})\exp(-|r|^2/2r_0^2)$, is $\hat{J}(\xi) = \exp(-r_0^2|\xi|^2/2)$. Thus, suitable β, u_0, and ξ's give rise to a positive eigenvalue ω and subsequent exponential growth of the coverage u (eventually controlled by the exclusion principle), which leads to the formation of clusters.

2C. Mesoscopic Theories for Multiple Micromechanisms

Typically, multiple surface processes take place simultaneously, and one of the practical advantages of the mesoscopic theories is that they can be easily modified, combining the various spin flip/exchange mechanisms described earlier. Here we present a straightforward generalization of the mesoscopic theory developed in [7] (see also [13]). We consider Arrhenius adsorption/desorption dynamics, Metropolis surface diffusion, and a simple unimolecular reaction; the corresponding mesoscopic local mean field equation is

$$u_t - D\nabla \cdot [\nabla u - \beta u(1-u)\nabla J_m * u] - [k_a p(1-u) - k_d u \exp(-\beta J_d * u)] + k_r u = 0. \tag{2.9}$$

Here J_d and J_m are the intermolecular potentials for surface desorption and migration. Furthermore, D is the diffusion constant; k_r, k_d and k_a denote, respectively, the reaction, desorption, and adsorption constants; and p is the partial pressure of the gaseous species (k_d, k_a, and p are algebraically related to the parameters c_0 and h in (2.2)). Finally, u denotes the surface coverage of the adsorbed species.

The Fickian diffusion case is an interesting extreme ($J_m = 0$) typically adopted in diffusion–reaction models at the continuum and microscopic levels [22, 24, 37].

$$u_t - D\nabla u - [k_a p(1-u) - k_d u \exp(-\beta J_d * u)] + k_r u = 0. \tag{2.10}$$

The steady states of Eqs. (2.9) and (2.10) are the same as those of Eqs. (2.1) and (2.2), and thus the phase diagram in Fig. 2 also holds here with $\alpha = \frac{k_a p}{k_d}$ and $\lambda = J_0\beta$. When $J_d = J_m$ and $k_r = 0$, (2.1), (2.2), and (2.9) also share the same standing wave. However, there are no general rigorous results available on the existence of travelling waves for (2.9); some numerical simulations for identical interaction potentials $J_m = J_d = J$ were carried out in

[7], indicating the existence of nonmonotone travelling waves. Finally, it is easy to see that the free energy $E[u]$ is a Lyapunov functional for (2.9).

Clearly we can also consider variants of (2.9) with Arrhenius diffusion dynamics. Furthermore, it is possible to include fluctuations in the mesoscopic equations we discussed, derived directly from each of the micromechanisms, and satisfying fluctuation–dissipation relations [7, 9]; see also Appendix A. The role of fluctuations is critical, for instance, in nucleation and spinodal decomposition, and we extend the spectral methods presented here to stochastic mesoscopic equations in [D. Horntrop, M. Katsoulakis, and D. Vlachos, in preparation].

2D. Macroscopic Limits and Interface Dynamics

Some aspects of the complex relations between the above micro-, meso-, and macroscopic models were explored in [5–7, 9, 11, 13, 26, 27] (and references therein), where the authors have derived macroscopic PDEs, describing evolving clusters formed under the influence of attractive microscopic interactions. We also refer to the review article [33] for many other related references. In [6] it was shown that stochastic Ising models with spin flip dynamics yield evolving clusters moving with normal velocity which is a (possibly anisotropic) function of the principal curvatures of their boundaries. This function is actually described by a Kubo–Green-type formula which also specifies the relationship between the mobility and the surface energy of the propagating cluster boundaries on one hand, and the microscopic interaction potential and microscopic dynamics of the Ising model on the other. All these results are valid globally in time, the motion of the interface being interpreted in the viscosity sense after the onset of the geometric singularities. In [13] similar results were obtained for Eqs. (2.9) and (2.10), when multiple surface mechanisms coexist and interact. Finally, in [11] it was formally shown that the Kawasaki/Metropolis dynamics with isotropic potentials give rise to a Mullins–Sekerka free boundary problem with surface tension identified through the microscopic Hamiltonian. This last result was rigorously established for smooth Mullins–Sekerka flows in [E. Carlen, M. Carvalho, and E. Orlandi, in preparation]. We revisit some of these results in Section 4, where we compare them to our simulations.

3. NUMERICAL SCHEMES

Given the highly nonlinear nature of the mesoscopic model equation in (2.9), it is natural to use numerical methods in order to study such an equation. In light of the wide variety of physically relevant problems that can be described by (2.9), it is important that the numerical scheme be efficient and highly accurate. In particular, we are interested in numerical schemes which will allow for longer time evolutions involving greater length scales than are possible with Monte Carlo simulations while incorporating molecular effects that are not considered by macroscopic, phenomenological models.

The two main steps in devising a numerical scheme for (2.9) are the determination of the technique used to calculate the convolutions and the method for numerically solving the differential equation once the appropriate convolutions have been computed. Two natural approaches to these steps would be related to finite difference or lattice-based methods and spectral methods. While finite difference methods have been previously applied to mesoscopic models by two of the authors [13] as well as others [7, 20], we are unaware of the prior application of spectral methods in this context, though such methods have been

applied to a phenomenological model equation for 2D turbulence that has some features in common with our mesoscopic model [41], and a hybrid method has been applied in a study of the Ginzburg–Landau equations [52, 53]. We briefly describe each of these approaches in turn below and make performance comparisons at the end of this section.

3A. Finite Difference Methods

The basis of finite difference methods is the discretization of the physical domain into a lattice or array of points at which the solution of the problem is computed. The lattice points are chosen here to be equally spaced with spacing Δx and Δy. The first task in applying a finite difference method to (2.9) is to determine a means of calculating the value of the convolution integrals at each lattice site. One such approach would be to use a traditional numerical integration technique such as the trapezoid rule. However, it is well known (see [42], for example) that numerical integration of multiple integrals is much less efficient than that of single integrals; thus, the calculation of the convolutions needed at every node point for each time step will prove to be a computational bottleneck, unless more sophisticated techniques are employed. In the following paragraphs, we briefly describe some approaches used in the literature to reduce the computational time needed to calculate such convolutions. We also discuss why these approaches, while certainly an improvement of the standard quadrature technique, are still limited in applicability.

One set of such methods takes advantage of properties of the migration and desorption potentials J_m and J_d to simplify the calculation. For instance, for rapidly decaying potentials, i.e., potentials with relatively short correlation ranges, it is possible to calculate the convolution integral using only those grid points located within a small circle of the point about which the convolution is being computed, since the integrand is essentially zero beyond this circle. The radius of this circle is typically referred to as the cutoff distance of the potentials. Lists of neighbors can be maintained to speed up the calculation of the convolution [1] at the expense of larger memory requirements. Of course, while the determination of the neighbors of each point does require some initial computational time, the amount of computational time required for each time step is greatly reduced for potentials with short-range correlations. However, the storage requirements rapidly become quite large when large neighborhoods are required for accuracy, in complete analogy to molecular dynamics and Monte Carlo simulations.

Another physical space approach that could be taken in the calculation of the convolution integrals is to use a Gaussian quadrature technique. The main disadvantage of such an approach is that the integration nodes do not correspond with the lattice sites, thus inducing an interpolation error in determining the function values away from the lattice sites. An approach similar to Gaussian quadrature, which, in contrast, requires equispaced integration nodes, has been used in [43] to calculate convolution integrals with Gaussian potentials with a localized formula which is well suited for parallel computations. The greatest drawback to this technique is the specificity to Gaussian potentials; if other (possibly anisotropic) potentials were to be considered, the quadrature formula would have to be rederived and could even require a more complicated, less localized form.

The other main step in creating a finite difference scheme for (2.9) is making an appropriate discrete approximation to the underlying PDE. Since (2.9) is nonlinear and parabolic, it is reasonable to consider an explicit method which replaces the spatial derivatives with centered difference formulas and the temporal derivative with a forward difference [44, 45].

Thus, neglecting any errors in the calculation of the convolutions, such a method would have order 1 accuracy in time and order 2 accuracy in space.

Another important issue in the use of finite difference methods is the choice of time step Δt relative to the mesh spacing Δx and Δy to ensure the numerical stability of the algorithm. While it is possible to determine an explicit stability criterion for the linearized version of (2.9), with the convolutions replaced by the asymptotic expansion in (B.1), such a formula is quite complicated and is effectively a modification of the standard stability criterion for the heat equation: $\frac{D\Delta t}{(\Delta x)^2} + \frac{D\Delta t}{(\Delta y)^2} \leq \frac{1}{2}$ [44, 45]. Thus, in addition to the large number of computations needed at every time step just to compute the convolutions, a very small time step is necessary for numerical stability.

3B. Spectral Methods

Spectral methods are a class of numerical schemes that take advantage of many properties of Fourier transforms, especially the fact that differentiation in physical space corresponds to a multiplication in Fourier space. The computational efficiency of a spectral method relies upon the existence of the fast Fourier transform (FFT) to pass between physical space and Fourier space [46, 47]. We take the Fourier transform of (2.9) in spatial variables and thereby reduce the very complicated PDE (2.9) to a first-order nonlinear ordinary differential equation (ODE),

$$\hat{u}_t = (-k_a p - k_r - 4\pi^2 D|\xi|^2)\hat{u} + \widehat{F(u)}, \tag{3.1}$$

where ξ is the Fourier space variable and $\widehat{F(u)}$ is the spatial Fourier transform of

$$F(u) = k_a p - D\beta\nabla \cdot (u(1-u)\nabla J_m * u) - k_d u \exp(-\beta J_d * u). \tag{3.2}$$

The numerical calculation of $\widehat{F(u)}$ proceeds in a rather straightforward manner through the use of FFTs and the fact that convolutions are merely products in Fourier space. For instance, the Fourier space representation of the last term in (3.2) can be numerically computed by multiplying $\hat{J}_d$ and $\hat{u}$, transforming back to physical space for exponentiating and multiplying by u, and finally transforming back to Fourier space. Therefore, the computational problem reduces to the solution of a first order nonlinear ordinary differential equation with a forcing function which can be calculated rather efficiently at every point of the lattice for every time step. The accuracy of the calculation of the forcing function will also be rather high given the exponential accuracy of spectral methods.

Thus, we wish to select an ODE solver that is straightforward to implement for nonlinear equations, has a high level of accuracy, and has good stability properties. Given the relative ease of use of explicit methods for nonlinear equations, we selected the second order accurate Heun's method to solve the resulting ODE in (3.1). Heun's method uses an Euler predictor and a trapezoidal corrector and, as would be expected of any explicit method, has potentially strict time step requirements for numerical stability. The stability analysis of this method applied to (3.1) with F linearized and convolutions replaced by (B.1 (see Appendix B)) indicates that the nonlinear terms tend to lessen the severity of the time step restriction imposed by the displayed linear term in (3.1) for some parameter regimes; however, in general, it is prudent to use the stricter limitation $(k_a p + k_r + 4\pi^2 D|\xi|^2)\Delta t \leq 2$. Note that since the largest possible value of $|\xi|^2$ is essentially $\frac{1}{(\Delta x)^2} + \frac{1}{(\Delta y)^2}$ this time step restriction is basically as severe as required by the finite difference method. Thus, this most

straightforward spectral approach would result in a potential increase in computational speed and improved accuracy only in the calculation of the nonlinear terms at each time step as compared with the finite difference approach. Of course, in both approaches the time step restriction could be greatly reduced or even eliminated through the use of an implicit method; the major difficulty in using such an integrator would be the rather high computational cost of solving nonlinear equations at each time step.

However, since the severity of the time step restriction is predominately caused by the presence of the term multiplying $\hat{u}$ in (3.1), the elimination of this term should allow for the use of much longer time steps. The use of the integrating factor

$$\rho(t) = \exp[(k_a p + k_r + 4\pi^2 D|\xi|^2)t] \tag{3.3}$$

exactly treats this term and thereby allows the use of a larger time step while still avoiding numerical instabilities [46]. In detail, we multiply Eq. (3.1) by the integrating factor and obtain

$$(\rho(t)\hat{u})_t = \rho(t)\widehat{F(u)}. \tag{3.4}$$

The application of Heun's method to the ODE (3.4) gives

$$\begin{aligned}
\hat{\tilde{u}}(t_{n+1}) &= \rho(-\Delta t)(\hat{u}(t_n) + \Delta t \widehat{F(u)}(t_n)), \\
\hat{u}(t_{n+1}) &= \rho(-\Delta t)\hat{u}(t_n) + \frac{\Delta t}{2}[\rho(-\Delta t)\widehat{F(u)}(t_n) + \widehat{F(\tilde{u})}(t_{n+1})].
\end{aligned} \tag{3.5}$$

The formula in (3.5) demonstrates the explicit and exact calculation of the linear terms; it also shows the damping at the largest wave numbers that would be expected by a diffusion term as indicated by the dispersion relationship in (2.8).

In careful numerical studies, we have observed no significant loss of accuracy in many situations by when we used a time step that is one order of magnitude larger than would be required if we had not used the integrating factor. However, in situations where large wave number effects are important, the use of a large time step tends to prevent the formation of small-scale structures at short times; such behavior is reasonable as can been seen by considering the integrating factor in (3.3) and the discretized scheme in (3.5). (For large ξ and Δt, the quantity $\rho(-\Delta t)$ is quite small.) While this suppression of small-scale perturbations at short times does not necessarily change quantitative features of the results at later times, such as the statistical measures of the size of the typical length scale discussed in Section 4, the concentration configurations will typically appear to be qualitatively different even with the same initial data. Another situation in which it would be potentially inadvisable to take significantly larger time steps than allowed by the standard stability analysis for a spectral method without the integrating factor is when the balance between the migration term and the standard diffusion term is rather sensitive to perturbation. The stabilizing scheme proposed in [54] could potentially be applied here to resolve the inherent stiffness in the problem for long time calculations. All results given in this paper have been carefully validated to insure that an appropriate time step has been used. In the remainder of this paper, the term spectral method refers to use of the spectral method in conjunction with an integrating factor.

It is important to point out that it is possible to make the time steps in physical space rather than Fourier space in a spectral-based approach; however, for the model being studied here, there is no particular advantage to doing so since both u and $\hat{u}$ are needed at every

time step. Another noteworthy point is that the spectral method as described above assumes periodic boundary conditions; the use of Chebyshev polynomials allows the use of other types of boundary conditions [46, 47].

3C. Comparison of Numerical Schemes

We now compare the computational performance of the finite difference scheme and the spectral scheme described above. For the purposes of this comparison, we assume that the system is nonreactive ($k_r = 0$) and that there is no surface diffusion ($D = 0$); thus, (2.9) reduces to

$$u_t - [k_a p(1-u) - k_d u \exp(-\beta J_d * u)] = 0. \tag{3.6}$$

This case is attractive for computational comparisons for several reasons. This problem contains the main features of the complete model including the appearance of convolution in a nonlinear term as well as the possibility of spinodal decomposition; (see Section 2). The removal of the Fickian diffusion eliminates the obvious advantage in time step size Δt of the spectral method due to the use of the integrating factor and allows for a direct comparison of the accuracy and speed of the convolution calculation in an environment that is similar to that of the complete model (2.9).

For the purposes of this comparison, the finite difference scheme implements the calculation of the convolutions using the "neighborhood" technique described earlier. The effect of the size of the neighborhood on computational speed and accuracy is certainly an important aspect of our comparisons below. For the spectral scheme, we use the Euler method rather than Heun's method so that comparisons are being made between methods which are both order 1 in time. The desorption potential is a Gaussian given by

$$J_d(r) = \frac{1}{\sqrt{2\pi r_0^2}} \exp\left(\frac{-|r|^2}{2r_0^2}\right). \tag{3.7}$$

All physical parameters are selected to be the same in both cases: $k_a = 1$, $p = 1$, $k_d = 20$, $\beta = 5.7$, and $r_0 = .02$. The computational parameters are the same as well: $\Delta x = \Delta y = \frac{1}{128} = \frac{1}{N}$ and $\Delta t = .001$. Comparisons are made after 500 time steps from an initial configuration in which u is 1 inside a circle of radius $\frac{1}{6}$ and exponentially decays rapidly to 0 outside the circle.

The timing of the codes was completed on an SGI Octane workstation with an R10000 processor and is given in Table I with execution times rounded to the nearest second. The ℓ given for the finite difference results refers to the radial distance in terms of number of neighbors from the point about which the convolutions are being computed. For instance, $\ell = 3$ means that all lattice points within a circle of radius $3\Delta x$ are used in the calculation of the convolution. As can be seen from Table I, even the $\ell = 3$ neighbor finite difference code required four times as long to complete as did the spectral code; the difference became much more pronounced as ℓ increased. These timing results also agree with the estimates that would be obtained by considering operation counts for the calculation of the convolution since that is the most computationally demanding part of either code. For the spectral code, the calculation of the FFTs needed for the convolution takes $O(N^2 \log(N))$ and is the dominant factor in the computation time since the actual convolution itself is only $O(N^2)$. On the other hand, the finite difference code must calculate N^2 convolutions, each with

TABLE I

Comparison of the Computation Times for the Solution of (3.6) Using Various Techniques

Technique	Time
Spectral	1:50
Finite difference, $\ell = 3$	7:33
Finite difference, $\ell = 4$	13:03
Finite difference, $\ell = 5$	21:36
Finite difference, $\ell = 6$	30:24
Finite difference, $\ell = 7$	40:44

Note. The time is given in terms of minutes:seconds and is rounded to the nearest second.

$O(\ell^2)$ neighbors, and is thus roughly $O(N^2\ell^2)$. The appropriateness of this quantity to describe the computational time of the finite difference scheme can be seen by considering Table I; doubling ℓ from 3 to 6 required almost exactly four times more computational time, as predicted.

However, in order to get a complete picture for comparison, it is also important to consider the relative accuracy of the results. Given that, for the choice of r_0 and Δx used here, $\ell = 5$ would encompass roughly two standard deviations for the potential, it is not surprising that the results for $\ell < 5$ were quite different than the spectral results. On the other hand, for $\ell = 6$ the difference between the finite difference results and the spectral results was of order 10^{-3} for a typical lattice site; for $\ell = 7$, the difference was only of order 10^{-4}. Thus, referring to Table I we see that the finite difference approach requires more than an order of magnitude additional computational time in order to achieve results comparable to those of the spectral method. Even for much smaller values of r_0 (much shorter range potentials) and thus smaller necessary values of ℓ, there would still be a noticeable difference in computational time required; on the other hand, potentials with longer range correlations (larger r_0) would require much larger ℓ for accuracy, making finite differences with standard quadratures for convolutions impractical.

Similar timing and accuracy considerations also hold for the model with $D \neq 0$. However, the fact that the spectral method with the integrating factor is still numerically stable with a time step one to two orders of magnitude larger than can be used in a finite difference scheme means that the spectral approach gives a two to three orders of magnitude reduction in computation time as compared with a finite difference scheme.

While it is possible to combine the two main approaches described above (e.g., convolve with a spectral method and then use finite difference on the underlying model equation), such a scheme should not provide any advantages over a purely spectral approach. Such an approach has been used in the literature in a study of the time-dependent Ginzburg–Landau equation [52, 53]. Certainly the computation time for finite differences would be reduced by having a faster means of calculating the convolutions; however, the potential speed-up resulting from the larger time steps that are possible by treating the equation spectrally with the integrating factor is completely lost in such a combination of approaches.

In the next section, we make comparisons with asymptotically predicted behaviors to further support the validity of our results. Given the clear computational advantage of the spectral method, we use it exclusively in the remainder of this paper.

4. SCALING AND GROWTH LAWS

In order to further validate the results obtained from the spectral simulations, we now describe some comparisons with various well known and widely accepted scaling and growth laws. The first of these comparisons is for the same model (3.6) that was considered in the timing comparisons in the previous section. For that model, Fig. 2 describes the behavior of the system for various combinations of system parameters. Near the line of stationary coexistence (the dotted line of Fig. 2), the normal velocity of the cluster boundaries is given by $V = -\mu\sigma\kappa$, where μ is the mobility, σ is the surface tension, and κ is the curvature. Both the mobility and the surface tension can be given by Kubo–Green formulas, as shown in [13]. Thus, on the line of stationary coexistence, the rate of decay of the size of the field R is directly proportional to the curvature and inversely proportional to the size of the field, i.e.,

$$\frac{dR}{dt} \sim -\frac{1}{R}. \tag{4.1}$$

A solution of this equation is of the form

$$R(t) = \sqrt{c_1 - c_2 t}. \tag{4.2}$$

Away from the line of stationary coexistence, the curvature effects are of lower order and the rate of change of the size of the system is directly proportional to the travelling wave speed; thus, R should be a growing linear function of t above the stationary coexistence curve and a decaying linear function below the stationary coexistence curve.

In order to try to observe these behaviors in our computer simulations, we initialized the concentration field with a circle centered at the origin within which the concentration is 1; outside this circle, the concentration exponentially decayed to 0. The physical parameters chosen here are $k_a = 1$, $p = 1$, $k_d = 20$, and $r_0 = .01$. Note that these physical parameters correspond to $\alpha = \frac{k_a p}{k_d} = .05$ and $\lambda = J_0\beta = \beta$ in the phase diagram in Fig. 2 since $J_0 = \int J_d(r)dr = 1$ for the potential in (3.7) regardless of the choice of r_0. The computational domain is a box with sides of length 1 with periodic boundary conditions. A 128×128 lattice is selected, making $\Delta x = \Delta y = \frac{1}{128}$, while the time step is $\Delta t = .02$. Figure 3 shows the behavior of the radius of the circle as time evolved; for each curve, the dots represent the simulated radius while the solid lines are the least squares fits of the data to the appropriate curves. The top curve in Fig. 3 is the radius of the circle for the value $\beta = 6.5$ which is above the line of stationary coexistence; the linear growth that was theoretically predicted is quite visible. Likewise, the linear decay that was predicted to occur below the stationary coexistence curve can be seen in the lowest curve in Fig. 3, which depicts the radius for $\beta = 5.7$. The middle curve is for $\beta = 6.0$, which is very near the stationary coexistence curve; the fit of the data to the predicted form of the solution in (4.2) is quite close. Note as well that the change in the radius occurred on a much slower time scale when in the parameter regime near the line of stationary coexistence, as predicted by asymptotic arguments in [13].

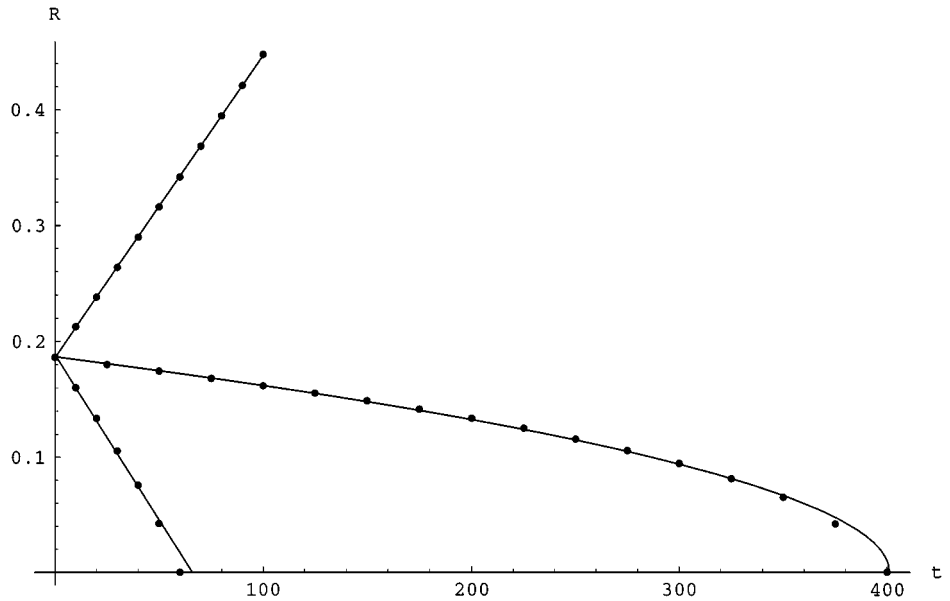

FIG. 3. Behavior of the radius of a circular patch of high concentration centered at the origin for various choices of β. The dots represent computed values while the solid lines represent least squares fits to appropriate functions. The top curve ($\beta = 6.5$) shows the linear growth predicted for β above the line of stationary coexistence; the middle curve ($\beta = 6.0$) agrees with the prediction in (4.2) for parameter regimes near the line of stationary coexistence; the bottom curve ($\beta = 5.7$) shows the linear decay predicted for β below the line of stationary coexistence.

It is also interesting to explore what happens to the above model when surface diffusion is present in the system, i.e., $D \neq 0$. In this case, the mesoscopic model equation takes the form

$$u_t - D\nabla \cdot [\nabla u - \beta u(1-u)\nabla J_m * u] - [k_a p(1-u) - k_d u \exp(-\beta J_d * u)] = 0. \quad (4.3)$$

Since there is no comparison principle for this model, it is not possible to rigorously derive results here that are similar to those obtained for the earlier model (3.6) using viscosity solution techniques. However, for small values of the diffusion constant D, the same asymptotic arguments do hold formally and thus we would expect to observe behavior similar to that observed for the model in (3.6) [13]. Here we consider a system near the stationary coexistence curve ($\beta = 6.0$) with the other physical parameters unchanged but with a slightly smaller time step $\Delta t = .01$. We select $J_m = J_d$ and initial data of the same form as before. Figure 4 contains a plot of the radius of the circle as a function of time for $D = 10^{-3}$, 10^{-4}, 10^{-5}, and 0 going from left to right. The dots are the actual radius from the computer run while the solid lines are the least squares fits of the data to curves of the form of (4.2). Thus we see that curvature effects still determine the decay of the system for small diffusion constants, though it is clear that the diffusion mechanism will come to dominate the results for larger diffusion constants.

An additional physical situation relating to the model in (4.3) that we explore numerically is the merger of clusters of high concentration when the diffusion constant D is small compared to the adsorption/desorption constants. In the parameter regime above the stationary coexistence line, circular patches that are initially large enough relative to the correlation

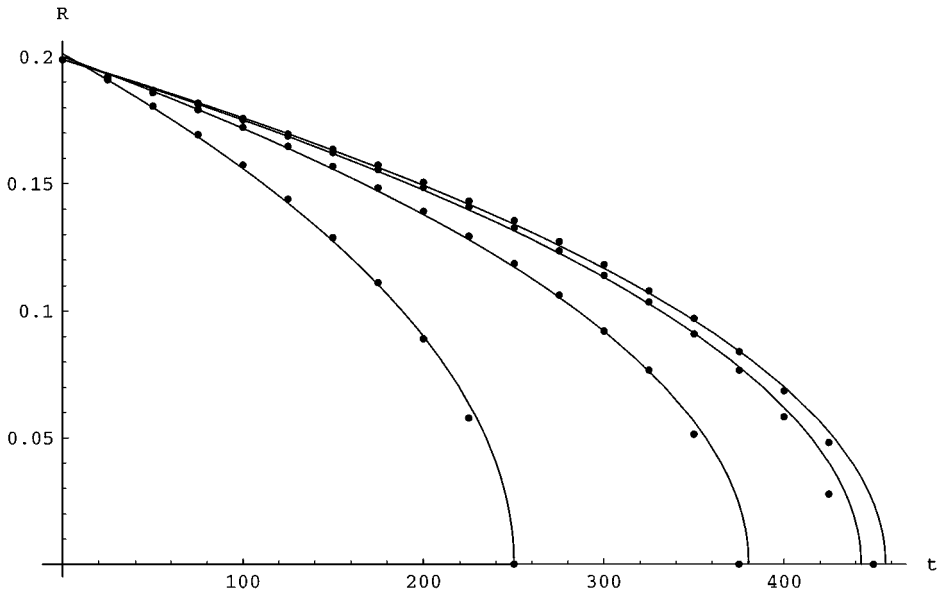

FIG. 4. The effect of diffusion on the decay of the radius of a circular patch of high concentration centered at the origin in a parameter regime near the line of stationary coexistence. From left to right, the curves are for the diffusion constants $D = 10^{-3}, 10^{-4}, 10^{-5}$, and 0. In all cases, the radius decayed as predicted by (4.2); however, this formal asymptotic prediction will not hold for large values of D.

length r_0 of the migration and desorption potentials such that the circular regions persist and grow in time would eventually meet at a single point, thereby creating a singularity beyond which asymptotic arguments could only hold formally. Past this initial meeting, formally one would expect the boundary to have a pair of cusp-like structures until the merger is complete. The sharpness of these cusps should be greater in parameter regimes further from the stationary coexistence line for the following two reasons: (1) Curvature effects start becoming more important when the parameters are near the stationary coexistence curve because the effect of curvature on the velocity of the boundary is no longer negligible when compared to the travelling wave speed, i.e., the enhanced velocity of the boundary at high curvature locations will tend to smooth the boundary; (2) the travelling wave transition front between high concentration and low concentration tends to be much steeper away from the stationary coexistence curve.

Figure 5 contains computational results which confirm the behavior described in the preceding paragraph. These computations used the same parameters used for Fig. 4 with the additional choice $D = 10^{-4}$. The initial data consisted of a pair of circles centered on the x-axis at $x = \pm.15$; the concentration field was set to be 1 inside these circles and exponentially decayed to 0 outside the circles. The plots in Fig. 5 are contour plots of the concentration function with lighter shading representing higher concentrations; the displayed contours represent concentrations of .1, .5, and .9. We consider the circles to have merged when the contours corresponding to a concentration of .5 have touched. The top two plots in Fig. 5 are for $\beta = 6.1$, which is relatively close to the stationary coexistence curve ($\beta \approx 6$ for our choice of k_d, k_a, and p) so that the curvature effects should be important; on the other hand, the bottom two plots in Fig. 5 are for $\beta = 7$, which is much further from the stationary coexistence line, making curvature effects negligible. The left-hand plots on

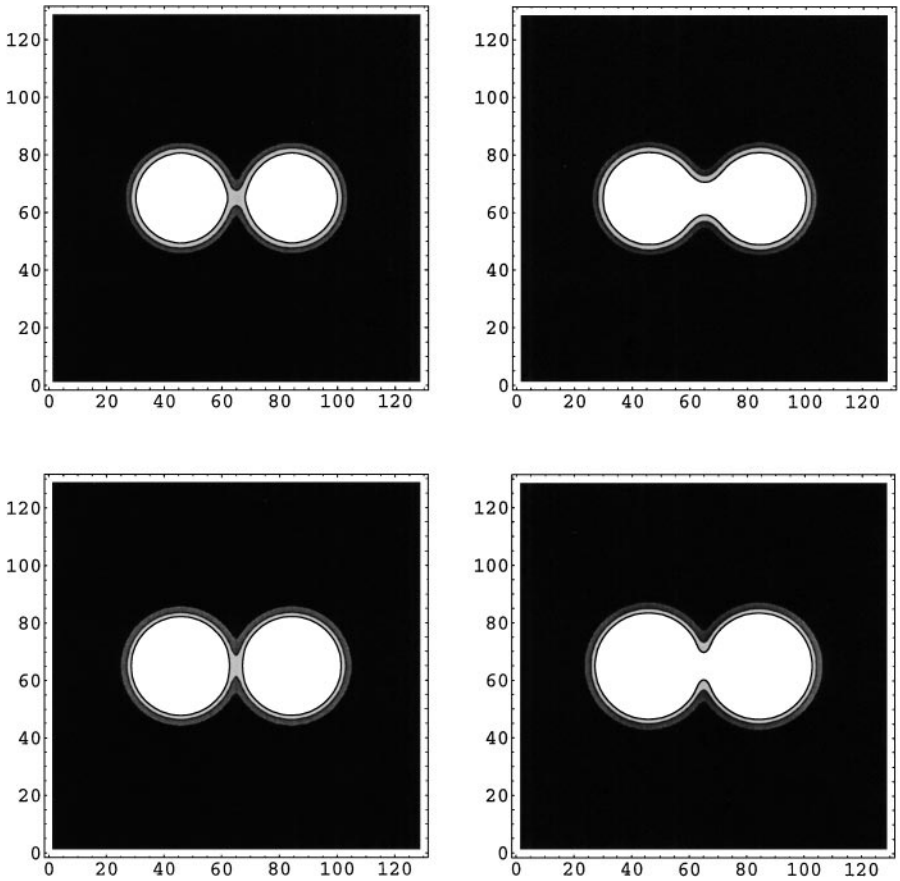

FIG. 5. Contour plots showing the effect of β on growing and merging circular patches of high concentration in parameter regimes above the line of stationary coexistence ($\beta \approx 6$ for our parameter choices). The top two plots are for $\beta = 6.1$, while the lower two plots are for $\beta = 7.0$. The left-hand plots are for a time just after the circles have begun to merge; the right-hand plots are for a comparable later time. The top plots show the smoothing of corners that would be expected in parameter regimes close to the statrionary coexistence curve; the lower plots have much sharper points on the boundary.

each row depict the system just after the circles have begun to merge, while the right-hand plots correspond to comparable later times. Even just after the merger, the tendency of the curvature effects to smooth the boundary are already observable; at the later times depicted in the right-hand plots, the smoothing of the interface where the two circles are merging is quite noticeable. Thus, our computations are in agreement with the formal asymptotic predictions.

We now consider the mesoscopic model equation for the Kawasaki dynamics from (2.9) with only the diffusion term, i.e., there is no adsorption, desorption, or reaction in the system.

$$u_t - D\nabla \cdot [\nabla u - \beta u(1-u)\nabla J_m * u] = 0. \tag{4.4}$$

This model is interesting to study because of the conservation of mass property for such a system. This property is an essential feature of a nucleating system if the Lifshitz–Slyosov growth law is to hold [48]. This law states that the typical length scale R in a nucleating

system grows like the power law t^n where $n = \frac{1}{3}$ at intermediate times, i.e.,

$$R \sim t^{\frac{1}{3}}, \tag{4.5}$$

while it has been shown that a Mullins–Sekerka free boundary problem arises at later times [11, 49]. However, here we merely wish to observe the Lifshitz–Slyosov growth law at intermediate times as a means to confirm that this law holds for (4.4) as well as to validate our computational work. While the law in (4.5) was originally derived for very dilute systems in which there is conservation of mass, it has been argued that such growth behavior should also be observed in nondilute systems as well; see [50, 51] and references therein. Thus, we are not restricted to considering only highly dilute systems.

The typical way one proceeds in order to observe such a scaling behavior in a computational study is to initialize the concentration field to a constant value with some random perturbation at each lattice site and then to evolve according to the underlying model equation, which is (4.4) here. Thus, the concentration field at any given moment in time may be thought of as one realization of a random field. Below we introduce some statistical quantities that describe the underlying structure of the concentration field; they are described for a single realization though each of the quantities is further refined through averaging over several realizations.

In order to measure the typical length scale in our concentration field, we need to look at statistical quantities such as the covariance and spectral density function of the concentration. These statistical quantities have also been used in studies of the Cahn–Hilliard equation in [16, 50, 51] and are described in greater detail in those references. (Note that the spectral density function has been referred to as the structure function in those references, while the term "structure function" has a different meaning in the stochastic processes and turbulence literature.) For a single realization of the concentration field, the covariance of the concentration is defined as a spatial average over the lattice sites,

$$B(x, t) = \frac{1}{N^2} \sum_{x'} u(x' + x, t)u(x', t) - \langle u \rangle^2, \tag{4.6}$$

where $\langle u \rangle$ is the mean of the concentration field, which is a constant for (4.4) due to conservation. For isotropic systems in which B depends only on the radial distance $r = |x|$, the covariance can be further simplified to a function of a single spatial variable by averaging over spherical shells.

One way to determine the typical length scale of the concentration field is to look at the Fourier transform of the covariance field which is the spectral density function

$$S(\xi, t) = \widehat{B}(x, t). \tag{4.7}$$

Again, for isotropic systems, the spectrum will depend only upon the magnitude of the wave number vector $|\xi|$. The value of the wave vector at which the spectrum has its maximum value would then correspond to the typical length of the concentration field. However, such a quantity can be difficult to calculate numerically; thus we will consider the first moment or mean of the spectral density function as a measure of the typical length scale of the system.

For our discrete system, the first moment can be written

$$\xi_1(t) = \frac{\sum_\xi \xi S(\xi, t)}{\sum_\xi S(\xi, t)}, \tag{4.8}$$

when the sum in the denominator serves to normalize the spectral density function. Given the inverse relationship between length scales in physical space and wave numbers in Fourier space, the Lifshitz–Slyosov growth law in (4.5) will take the form

$$\xi_1(t) \sim t^{-\frac{1}{3}}. \tag{4.9}$$

We now describe our numerical results in observing the Lifshitz–Slyosov growth law for the model in (4.4). The concentration field was initialized with perturbations of amplitude .05 about a fixed value of .25. The migration potential J_m is chosen to be a Gaussian of the same form as (3.7) with the choice $r_0 = .01$. The other physical parameters used include $\beta = 6$ and $D = 1$. The lattice is the same as for the other results in this section while the time step is $\Delta t = .0001$. Figure 6 contains a log–log plot of $\xi_1(t)$ versus t. The dots represent numerically computed values of $\xi_1(t)$ while the solid line has slope $-\frac{1}{3}$ and is given for visual reference purposes. The start-up effects at short times can be clearly seen before the system eventually settles down to the scaling behavior predicted by the Lifshitz–Slyosov growth law in (4.9). The least squares fit on the data values in the appropriate asymptotic regime yield a scaling exponent of $-.33 \pm .02$, which closely agrees with the predicted value of $-\frac{1}{3}$. Thus, we have confirmed that the Lifshitz–Slyosov law holds for the model in (4.4) with Kawasaki dynamics as well as further validated our computational scheme. In

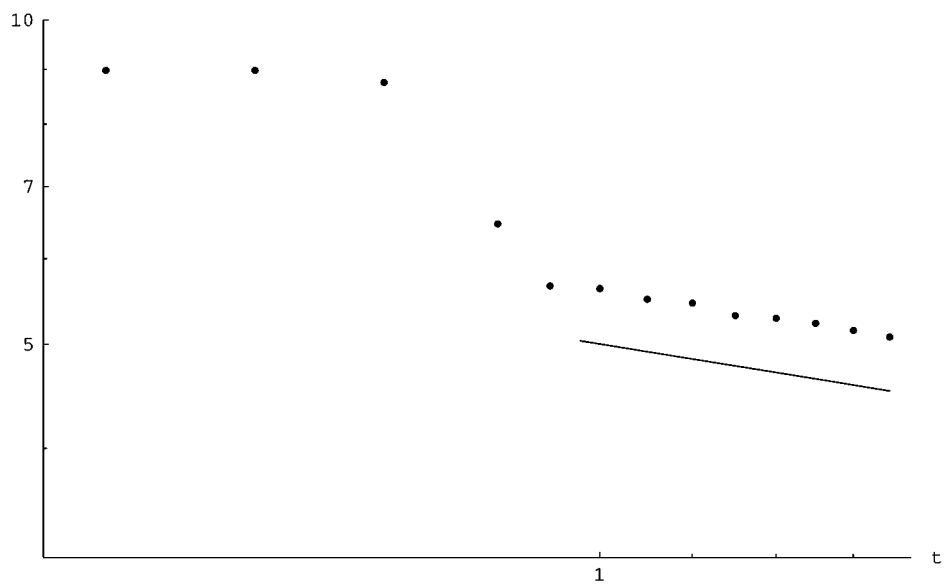

FIG. 6. Log–log plot of the mean value of the spectral density function versus time. The solid line has slope $-\frac{1}{3}$ and is useful for a visual comparison of the computation with the predicted value from the Lifshitz–Slyosov growth law. After some start-up effects, the calculated results clearly scale as predicted; the least squares fit of the exponent is -0.33 ± 0.02.

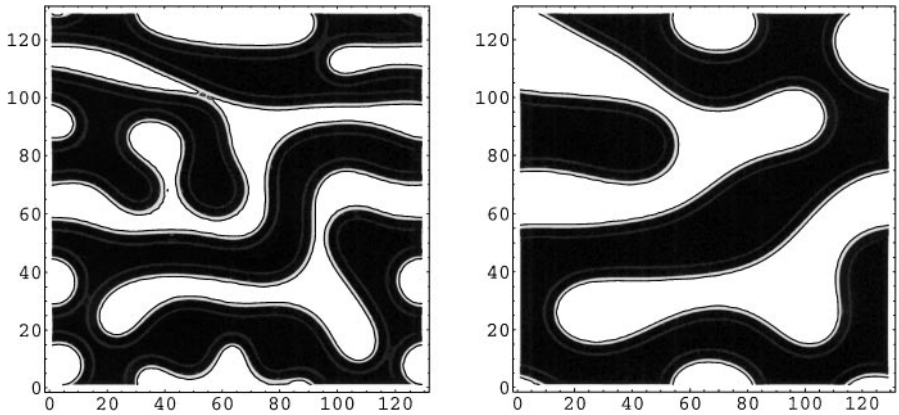

FIG. 7. Contour plots containing examples of the morphology obtained for the model (2.9) with k_r nonzero. Both plots are for the same initial data but the right-hand plot is for a later time than the left-hand plot. The right-hand plot demonstrates the tendency of the labyrinths to organize into larger scale structures at later times.

future work, we will explore similar issues for mesoscopic models with Arrhenius dynamics as well as (2.9).

So far in this section, we have validated our spectral method by making comparisons of our computational results with derived asymptotic results. In all cases, the simulation results were in excellent agreement with the theoretical prediction. Thus, combined with the comparisons made in Section 3 with a finite difference numerical scheme, we see that the spectral method is indeed a very powerful and reliable numerical approach to the solution of mesoscopic models. Finally, we briefly mention some of the results that are obtainable with our spectral scheme in other parameter regimes, such as when the reaction rate k_r is nonzero; in such a case complex patterns tend to develop [20]. A typical example computed in this case can be seen in Fig. 7 where a labyrinthine pattern is observed; the plot on the right is at a later time than the plot on the left. As we typically observe at later times in such simulations, the small structures tend to organize into larger structures and more regular patterns. Further details of such simulations will appear in future publications.

5. CONCLUSIONS

In this paper we have developed spectral-based algorithms for mesoscopic equations modeling surface processes and shown their greatly enhanced efficiency as compared to more traditional finite difference schemes. We validated the accuracy of the spectral schemes through comparison with asymptotic scalings and growth laws. We have also reviewed the derivation of mesoscopic models for pattern formation from the underlying microscopic mechanisms and discussed the connections of mesoscopic theories with well known models such as the Cahn–Hilliard equation and its variants.

Mesoscopic theories such as the ones discussed here in the context of surface processes are applicable to numerous areas including polymers, smart materials, biological systems, and complex fluids. We intend to further pursue the development of spectral schemes for such problems in future work.

APPENDIX A: DERIVATION OF MESOSCOPIC EQUATIONS

In this appendix, we outline the derivation of mesoscopic evolution equations from the underlying microscopic mechanisms. We begin with a description of some basic microscopic mechanisms arising in surface processes.

A1. Microscopic Models

Ising models are interacting particle systems defined on a d-dimensional lattice $\mathbb{Z}^d$. At each lattice site $x \in \mathbb{Z}^d$, an order parameter is allowed to take the values 0 and 1 describing vacant and occupied sites, respectively. In accordance to the classical Ising model, we refer to the order parameter as spin. A spin configuration σ is an element of the configuration space $\Sigma = \{0, 1\}^{\mathbb{Z}^d}$; we write $\sigma = \{\sigma(x) : x \in \mathbb{Z}^d\}$ and call $\sigma(x)$ the spin at x. The energy H of the system, evaluated at σ, is given by a Hamiltonian

$$H(\sigma) = \sum_{x \neq y} J(x, y)\sigma(x)\sigma(y) + h \sum \sigma(x),$$

where h is attributed to an external field and $J = J^\gamma$ is the intermolecular potential defined by

$$J(x, y) = J^\gamma(x, y) = \gamma^d J(\gamma(x - y)) \quad x, y \in \mathbb{Z}^d, \tag{A.1}$$

with $\gamma^{-1} > 0$ being the interaction range and J assumed to be even, $J(r) = J(-r)$. The scaling in (A.1) guarantees the summability of the Hamiltonian H, provided $J \in L^1(\mathbf{R}^d)$. If the microscopic interactions are attractive, i.e., J is nonnegative, then we say that the Ising model is ferromagnetic. In general, J may include a combination of both attractive and repulsive interactions.

Equilibrium states of the Ising model are described by the Gibbs states at the prescribed temperature T,

$$\mu_\Lambda(d\sigma) = \frac{1}{Z_\Lambda} \exp(-\beta H(\sigma))\, d\sigma, \tag{A.2}$$

where $\beta = \frac{1}{kT}$, k being the Boltzmann constant. Z_Λ is a normalizing constant so that μ is a probability measure defined on the configuration space $\Sigma = \{0, 1\}^\Lambda$, where Λ is an expanding (as $|\Lambda| \to \infty$) finite box on the infinite lattice, with specified boundary conditions. It is well known that phase transitions, i.e., nonuniqueness of the Gibbs measures, may occur at low temperatures, in the infinite volume limit [28].

The dynamics of the model consists of a sequence of flips and spin exchanges that correspond to various physical processes. We describe these microscopic mechanisms in detail below.

A1.1. *Adsorption/Desorption: Spin Flip Mechanism*

A spin flip at the site x is a spontaneous change in the order parameter; 1 is converted to 0 and vice versa. Physically this mechanism describes the desorption of a particle from the surface to the gas phase and conversely the adsorption of a particle from the gas phase to the surface (see Fig. 1).

If σ denotes the configuration prior to a flip at x, then after the flip the configuration is denoted by σ^x. We assume that a flip occurs at x, when the configuration is σ, with a rate $c(x,\sigma)$, i.e., a spin flip occurs at x, during $[t, t+\Delta t]$, with probability $c(x,\sigma)\Delta t + O(\Delta t^2)$. Rigorously, the underlying stochastic process $\{\sigma_t\}_{t\geq 0}$ is a jump Markov process on $L^\infty(\Sigma;\mathbf{R})$ with generator given by

$$L_\gamma^{ad} f(\sigma) = \sum_{x\in\mathbb{Z}^N} c(x,\sigma)[f(\sigma^x) - f(\sigma)], \quad f \in L^\infty(\Sigma;\mathbf{R}). \tag{A.3}$$

An obvious requirement on the resulting dynamics is that, when restricted on a finite dimensional box Λ, they should leave the Gibbs measure (A.2) invariant. This condition is called a *detailed balance* law and is equivalent to [29]

$$c(x,\sigma) = c(x,\sigma^x)\exp(-\beta\Delta_x H(\sigma)). \tag{A.4}$$

Here $\Delta_x H(\sigma) = H(\sigma^x) - H(\sigma)$ is the energry difference ater performing a spin flip at the site x. The simplest type of dynamics satisfying (A.4), referred to as Metropolis-type, is

$$c(x,\sigma) = \Psi(-\beta\Delta_x H(\sigma)), \tag{A.5}$$

yielding the relaiton on Ψ, $\Psi(r) = \Psi(-r)e^{-r}$, $r\in\mathbf{R}$. Typical choices of Ψ's are $\Psi(r) = (1+e^r)^{-1}$ (Glauber dynamics), $\Psi(r) = e^{-r/2}$, or $\Psi(r) = e^{-r^+}$ (Metropolis dynamics).

A1.2. *Surface Diffusion: Spin Exchange Mechanism*

A spin exchange between the neigbhoring sites x and y is a spontaneous exchange of the values of the order parameter at x and y. Physically this mechanism describes the diffusion of a particle on a flat surface (see Fig. 1). Note that sites cannot be occupied by more than one particle (exclusion principle). As in the spin flip dynamics, a spin exchange occurs with rate $c(x,y,\sigma)$ satisfying the detailed balance law

$$c(x,y,\sigma) = c\big(x,y,\sigma^{(x,y)}\big)\exp\big(-\beta\Delta_{(x,y)}H(\sigma)\big), \tag{A.6}$$

where $\sigma^{(x,y)}$ is the new configuration after a spin exchange between sites x and y. Furthermore, $\Delta_{x,y}H(\sigma) = H\big(\sigma^{(x,y)}\big) - H(\sigma)$ is the energy difference after performing a spin exchange between the neighboring sites x and y. The Hamiltonian H associated with diffusion may have a different intermolecular potential J than adsorption. The resulting stochastic process $\{\sigma_t\}_{t\geq 0}$ is a jump Markov process on $L^\infty(\Sigma;\mathbf{R})$ with generator given by

$$L_\gamma^{d} f(\sigma) = \sum_{x\in\mathbb{Z}^d} c(x,y,\sigma)\big[f\big(\sigma^{(x,y)}\big) - f(\sigma)\big]. \tag{A.7}$$

The Metropolis-type dynamics, which satisfy (A.6), is

$$c(x,y,\sigma) = \begin{cases} \Psi(-\beta\Delta_{x,y}H(\sigma)), & \text{when } x \text{ and } y \text{ are nearest neighbors,} \\ 0, & \text{otherwise,} \end{cases} \tag{A.8}$$

where $\Psi(r) = \Psi(-r)e^{-r}$, $r\in\mathbf{R}$. Typical choices of Ψ's are $\Psi(r) = 2(1+e^r)^{-1}$ (Kawasaki dynamics) and $\Psi(r) = e^{-r^+}$ (Metropolis dynamics).

A1.3. *Arrhenius Dynamics for Adsorption/Desorption and Surface Diffusion*

In most Monte Carlo simulations, motion of species is performed according to Metropolis or Kawasaki dynamics [1]. For such dynamics, the energy barrier for diffusion depends only on the energy difference between the initial and final states, often known as the heat of the process. Since the equilibrium state of a system is independent of dynamics, different choices of microscopic dynamics result in the same long time solution due to the detailed balance condition. However, time-dependent solutions and the time needed to approach equilibrium depend on the details of microscopic dynamics. It is then more natural to describe the activation energy of surface diffusion as the energy barrier a species has to overcome in jumping from one site to another [30, 31]. This activation energy corresponds (omitting the zero point energy difference for clarity) to the difference between the minimum and maximum energies shown in Fig. 1b. The adsorption/desorption mechanisms are handled similarly. Such dynamics is termed Arrhenius [9].

The Arrhenius adsorption/desorption (spin flip) rate is given by

$$c(x,\sigma)=\begin{cases} c_0\exp\left[-\beta(U_0+U(x))\right], & \text{when } \sigma(x)=1.\\ c_0, & \text{when } \sigma(x)=0.\end{cases}$$

The Arrhenius surface diffusion (spin exchange) rate is given for nearest neighbors x and y by

$$c(x,y,\sigma)=\begin{cases} c_0\exp\left[-\beta(U_0+U(x))\right], & \text{when } \sigma(x)=1, \quad \sigma(y)=0,\\ c_0\exp\left[-\beta(U_0+U(y))\right], & \text{when } \sigma(x)=0, \quad \sigma(y)=1,\\ 0, & \text{otherwise,}\end{cases}$$

where in both formulae

$$U(x)=\sum_{z\neq x} J(x-z)\sigma(z)$$

is the total energy contribution from the particle interactions with the particle located at the site x, while U_0 is the energy associated with the surface binding of the particle at x (c_0 is a rate constant that can be chosen arbitrarily). Both spin flip and spin exchange dynamics satisfy the detailed balance law. A more complex dependence of the activation energy on the energetics of adjacent sites is also possible, e.g., Arrhenius parabolic jump models [30, 31].

A2. Mesoscopic Models: Local Mean Field Equations

Here we briefly discuss the derivation of mesoscopic theories for each of the microscopic models we introduced above, as well as combinations of such mechanisms. At large space/time scales and for weak long-range potentials, the small-scale fluctuations of the Ising systems are suppressed and an almost deterministic pattern emerges described by suitable, possibly stochastic, integrodifferential equations. The passage in the limit $\gamma \to 0$ (the interaction range is γ^{-1}; see (A.1)), which in the physics literature is identified with coarse graining, of quantities like the thermodynamic pressure, total coverage, etc., is known as the Lebowitz–Penrose limit [32]. Along these lines we study the asymptotics, as $\gamma \to 0$,

of the averaged coverage

$$u_\gamma(x,t) = E_{\mu^\gamma}\sigma_t(x), \quad (x,t) \in \mathbb{Z}^d \times [0,\infty)$$

of the system, where E_{μ^γ} denotes the expectation of the IPS starting from a measure μ^γ. Similarly, one may study the related asymptotic limit of a suitable averaged in space occupation

$$v_\gamma(x,t) = \frac{1}{|B_x|}\sum_{y\in B_x}\sigma_t(y),$$

where B_x is a ball centered at x with radius $R = \gamma^{-a} \ll \gamma^{-1}$, where γ^{-1} is the interaction range and $0 < a < 1$. Through the scaling $R = \gamma^{-a}$, the ball B_x where the averaging is carried out contains enough points so that the random fluctuations will be suppressed due to the Law of Large Numbers, while at the same time spatial variations in the coverage are captured since the averaging is performed over regions relatively smaller than the interaction range. Thus, as $\gamma \to 0$, $u_\gamma(x,t) - v_\gamma(x,t)$ converges to zero; in addition there is a normally distributed correction to $v_\gamma(x,t)$ of order $O(\gamma^{d/2})$ as in the Central Limit Theorem. We refer to the review article [33] and references therein for some rigorous results on these asymptotic limits, while here we present only the formal derivation of the mesoscopic equations separately for each micromechanism.

A2.1. *Adsorption/Desorption: Spin Flip Mechanism*

The generator (A.3) yields that the averaged coverage $u_\gamma(x,t) = E_{\mu^\gamma}\sigma_t(x)$ solves

$$\frac{d}{dt}E_{\mu^\gamma}\sigma_t(x) = E_{\mu^\gamma}(1-2\sigma_t(x))c(x,\sigma_t). \tag{A.9}$$

When the interparticle potential is weak and long range, the fluctuations of $\sigma_t(z)$ around their averages are approximately independent, the Law of Large Numbers formally applies and, as $\gamma \to 0$,

$$\sum_{z\neq x} J(x-z)\sigma_t(z) \approx \sum_{z\neq x} J(x-z)E_{\mu^\gamma}\sigma_t(z). \tag{A.10}$$

In addition there is a normally distributed correction of order $O(\gamma^{d/2})$ in a d-dimensional lattice due to the Central Limit Theorem. Here we ignore such random corrections, but in principle they would give rise to a stochastic PDE instead of a deterministic equation. Back in (A.9), we substitute the spin flip rate, and using (A.10) we obtain, as $\gamma \to 0$, $u_\gamma(x,t) = E_{\mu^\gamma}\sigma_t(x) \approx u(\gamma x, t)$, and u solves [6] the mesoscopic equations (2.1) or (2.2) as given in Section 2 for each choice of microscopic dynamics.

A2.2. *Surface Diffusion: Spin Exchange Mechanism*

As above, the generator (A.7) yields that the averaged coverage $E_{\mu^\gamma}\sigma_t(x)$ solves

$$\frac{d}{dt}E_{\mu^\gamma}\sigma_t(x) = \sum_{y\in N(x)} E_{\mu^\gamma}(\sigma_t(y)-\sigma_t(x))c(x,y,\sigma), \tag{A.11}$$

where $N(x)$ denotes the nearest neighbors of x. Reasoning as in the adsorption/desorption case we also have that $\sum_{z\neq x} J(x-z)\sigma_t(z) \approx \sum_{z\neq x} J(x-z)E_{\mu^\gamma}\sigma_t(z)$. Rescaling time as $t \mapsto t\gamma^{-2}$ in (A.11) and using the approximate independence of different lattice sites for $\gamma \ll 1$, we obtain for the dynamics (A.8) that, as γ vanishes, $u_\gamma(x,t) = E_{\mu^\gamma}\sigma_{t\gamma^{-2}}(x) \approx u(\gamma x, t)$, and u solves [10] the mesoscopic model equations (2.4) in Section 2. Similarly we can handle the Arrhenius dynamics and obtain (2.5) [9].

When the microscopic fluctuations are retained it can be formally shown that the coarse-grained variable u^γ approximately solves the stochastic mesoscopic equation

$$u_t^\gamma - \nabla\cdot\left\{\mu[u^\gamma]\nabla\left(\frac{\delta E[u^\gamma]}{\delta u^\gamma} + h\right)\right\} - \gamma^{d/2}\nabla\cdot\left\{\sqrt{2\mu[u^\gamma]}\dot{W}\right\} = 0, \tag{A.12}$$

where the variational derivative and the mobilities μ are defined in Section 2B, d is the space dimension, h is the external field, γ^{-1} is the interaction radius of the potential J in (A.1), and $\dot{W} = \left(\dot{W}_1(x,t), \ldots, \dot{W}_d(x,t)\right)$ is a d-dimensional space/time white noise.

APPENDIX B: RELATIONSHIP OF MESOSCOPIC MODELS TO GINZBURG–LANDAU MODELS

In this appendix we briefly discuss the connections of the mesoscopic equations with well known models for phase separation such as the Allen–Cahn and the Cahn–Hilliard models. If we rescale space as $x \mapsto x/\epsilon$, the potential J gives rise to the approximation of the Dirac distribution $J^\epsilon(x) = \epsilon^{-d}J(\frac{x}{\epsilon})$. Then after a simple change of variables and formally expanding in Taylor series,

$$\begin{aligned} J^\epsilon * u(x) &= \int J(z)u(x+\epsilon z)\,dz \\ &= \int J(z)\left[u(x) + \epsilon\nabla u(x)\cdot z + \frac{\epsilon^2}{2}z^T\nabla^2 u(x)z + O(\epsilon^3)\right]dz. \end{aligned} \tag{B.1}$$

Ignoring the $O(\epsilon^3)$ terms and assuming that J is radially symmetric, i.e., $J(r) = J(|r|)$, we have that

$$J^\epsilon * u(x) \approx J_0 u(x) + \frac{\epsilon^2}{2}J_2\Delta u(x), \tag{B.2}$$

where $J_0 = \int J(r)\,dr$ and $J_2 = \int |r|^2 J(r)\,dr$. Then, for instance, (2.2) is approximated by a "porous medium" version of the Allen–Cahn equation

$$u_t = Du\exp(-\beta J_0 u)\Delta u + c_0[1 - u - \exp(-\beta h)u\exp(-\beta J_0 u)],$$

where $D = c_0\frac{\epsilon^2}{2}\beta J_0\exp(-\beta h)$. Note that, as discussed in Section 2, the function $\lambda^{-1}f(u) = 1 - u - \exp(-\beta h)u\exp(-\beta J_0 u)$ is bistable or equivalently is the derivative of a double-well potential when the parameters lie in Region III (see Fig. 2). We remind the reader that the Allen–Cahn equation has the nondimensional form

$$u_t = \Delta u + W'(u),$$

where W is the double-well potential $W(u) = (u^2-1)^2$ [39].

In the case of the surface diffusion we can rewrite the free energy (2.6) as

$$E[u] = \frac{1}{4}\int\int J(r-r')[u(r)-u(r')]^2\,dr\,dr' + \int W_\beta(u)\,dr.$$

$W_\beta(u)\frac{1}{2}J_0u(1-u) + \frac{1}{\beta}[u\ln u + (1-u)\ln(1-u)]$. W_β is a double-well potential provided $\beta > \beta_c = 4/J_0$. Note that W_β is also known in the polymer science literature as the Flory–Huggins free energy; see for instance [16]. Then, rescaling and expanding the convolution as before, we have that

$$E[u] \approx \tilde{E}[u] := \int \frac{\epsilon^2 J_2}{8}|\nabla u|^2 + W_\beta(u)\,dr,$$

after omitting the higher order terms. This is the standard Ginzburg–Landau functional, in which case (2.4) becomes a Cahn–Hilliard-type equation

$$u_t - \nabla\cdot\left\{\mu[u]\nabla\left(\frac{\delta\tilde{E}[u]}{\delta u}\right)\right\} = 0, \tag{B.3}$$

with nontrivial mobility $\mu(u) = Du(1-u)$; recall that in the standard Chan–Hilliard model $\mu(u) = 1$. Similarly, we may simplify the Arrhenius dynamics equation (2.5) which will have effective mobility $\mu(u) = Du(1-u)\exp(-\beta J_0 u)$.

The analogies pointed out here between the mesoscopic and the Cahn–Hilliard and Allen–Cahn equations hold when the underlying interaction potentials are attractive, as suggested by the expansions above. However, mesoscopic equations are applicable for any combination of attractive and repulsive interactions. Furthermore, as discussed in [55] and [6], respectively, the truncations in the gradient expansions disregard higher order effects as well as possible anisotropies in the potential J. In the vicinity of the critical temperature and for attractive interactions the Allen–Cahn and Cahn–Hilliard equations become exact rescaled limits of the mesoscopic models and the underlying particle systems [33]. Models similar to (B.2), with or without chemical reaction, have been used in the modeling of phase separation in polymer blends; see [15, 16, 40] and references therein.

ACKNOWLEDGMENTS

The research of DJH is partially supported by NSF DMS-0079536; the research of MAK is partially supported by NSF DMS-9626804, NSF DMS-9801769, and NSF DMS-0079536; and the research of DGV is partially supported by the NSF Career Award CTS-9702615.

REFERENCES

1. M. P. Allen and D. J. Tildesley, *Computer simulation of liquids* (Oxford Sci. Publ. Oxford, 1989).
2. S. Jakubith, H. H. Rotermund, W. Engel, A. Von Oertzen, and G. Ertl, Spatiotemporal concentration patterns in a surface reaction: Propagating and standing waves, rotating spirals, and turbulence, *Phys. Rev. Lett.* **65**, 3013 (1990).
3. T. B. Thompson, DOE workshop roadmap for computational chemistry, http://itri.loyola.edu/molmodel (1999).
4. J. L. Lebowitz, E. Orlandi, and E. Presutti, A particle model for spinodal decomposition, *J. Stat. Phys.* **63**, 933 (1991).

5. A. De Masi, E. Orlandi, E. Presutti, and L. Triolo, Glauber evolution with Kac potentials 1: Mesoscopic and macroscopic limits, interface dynamics, *Nonlinearity* **7**, 633 (1994).
6. M. A. Katsoulakis and P. E. Sougandis, Stochastic Ising models and anisotropic front propagation, *J. Stat. Phys.* **87**, 63 (1997).
7. M. Hildebrand and A. S. Mikhailov, Mesoscopic modeling in the kinetic theory of adosrbates, *J. Phys. Chem.* **100**, 19,089 (1996).
8. G. Giacomin and J. L. Lebowitz, Exact macroscopic description of phase segregation in model alloys with long-range interactions, *phys. Rev. Lett.* **76**, 1094 (1996).
9. D. G. Vlachos and M. A. Katsoulakis, Derivation and validation of mesoscopic theories for diffusion-reaction of interacting molecules, *Phys. Rev. Lett.* **85**, 3898 (2000).
10. G. Giacomin and J. L. Lebowitz, Phase segregation dynamics in particle systems with long-range interactions. I. Macroscopic limits, *J. Stat. Phys.* **87**, 37 (1997).
11. G. Giacmin and J. L. Lebowitz, Phase segregation dynamics in particle systems with long-range interactions. II. Interface motion, *SIAM J. Appl. Math.* **58**, 1707 (1998).
12. M. A. Katsoulakis and P. E. Souganidis, Generalized motion by mean curvature as a macroscopic limit of stochastic Ising models with long-range interactions and Glauber dynamics, *Comm. Math. Phys.* **169**, 61 (1995).
13. M. A. Katsoulakis and D. G. Vlachos, From microscopic interactions to macroscopic laws of cluster evolution, *Phys. Rev. Lett.* **84**, 1511 (2000).
14. J. W. Cahn and J. E. Hilliard, Free energy of a nonuniform system I: Interfacial free energy, *J. Chem. Phys.* **28**, 258 (1958).
15. Q. Tran-Cong and A. Harada, Reaction-induced ordering phenomena in binary polymer mixtures, *Phys. Rev. Lett.* **76**, 1162 (1996).
16. S. C. Glotzer, E. A. Di Marzio, and M. Muthukumar, Reaction-controlled morphology of phase-separating mixtures, *Phys. Rev. Lett.* **74**, 2034 (1995).
17. M. Motoyama and T. Ohta, Morphology of phase-separating binary mixtures with chemical reaction, *J. Phys. Soc. Jpn.* **66**, 2715 (1997).
18. R. Lam, T. Basak, D. G. Vlachos, and M. A. Katsoulakis, Validation of mesoscopic theories and their application to computing concentration-dependent diffusivities, submitted.
19. M. N. Kuperman and H. E. Troiani, Pore formation during dezincification of Zn-based alloys, *Appl. Surf. Sci.* **148**, 56 (1999).
20. M. Hildebrand, A. S. Mikhailov, and G. Ertl, Nonequilibrium stationary microstructures in surface chemical reactions, *Phys. Rev. E* **58**, 5483 (1998).
21. R. Imbihl and G. Ertl, Oscillatory kinetics in heterogeneous catalysis, *Chem. Rev.* **95**, 697 (1995).
22. G. Ertl, Oscillatory kinetics and spatio–temporal self-organization in reactions at solid surfaces, *Science* **254**, 1750 (1991).
23. G. H. Gilmer and P. Bennema, Simulation of crystal growth with surface diffusion, *J. Appl. Phys.* **43**, 1347 (1972).
24. D. G. Vlachos, L. D. Schmidt, and R. Aris, Effect of phase transitions, surface diffusion, and defects on heterogeneous reactions: Multiplicities and fluctuations, *Surf. Sci.* **249**, 248 (1991).
25. K. Binder, Ed., *Monte Carlo Methods in Statistical Physics* (Springer-Verlag, Berlin, 1986).
26. H. Spohn, Interface motion in models with stochastic dynamics, *J. Stat. Phys.* **71**, 1081 (1993).
27. E. Carlen, M. Carvalho, and E. Orlandi, in preparation.
28. D. Ruelle, *Statistical Mechanics: Rigorous Results* (Benjamin, New York/Amsterdam, 1969).
29. H. Spohn, *Large Scale Dynamics of Interacting Particles* (Springer-Verlag, Berlin/New York, 1991).
30. H. C. Kang and W. H. Weinberg, Dynamic Monte Carlo with a proper energy barrier: Surface diffusion and two-dimensional domain orderings, *J. Chem. Phys.* **90**, 2824 (1988).
31. H. C. Kang and W. H. Weinberg, Modeling the kinetics of heterogenous catalysis, *Chem. Rev.* **95**, 667 (1995).
32. A. De Masi and E. Presutti, *Mathematical Methods for Hydrodynamic Limits*, Lecture Notes in Mathematics, (Springer-Verlag, Berlin, 1991), Vol. 1501.

33. G. Giacomin, J. Lebowitz, and E. Presutti, Deterministic and stochastic hydrodynamic equation arising from simple microscopic model systems, in *Stochastic Partial Differential Equations: Six Perspectives*, edited by R. Carmona and B. Rozovskii, Mathematical Surveys Monographs (Am. Math. Soc., Providence, 1999), Vol. 64, p. 107.
34. X. Chen, Existence, uniqueness, and asymptotic stability of traveling waves in nonlocal evolution equations, *Adv. Differential Equations* **2**, 125 (1997).
35. A. De Masi, T. Gobron, and E. Presutti, Travelling fronts in nonlocal evolution equations, *Arch. Rational Mech. Anal.* **132**, 143 (1995).
36. P. Bates, P. Fife, X. Ren, and X. Wang, Traveling waves in a convolution model for phase transitions, *Arch. Rational Mech. Anal.* **138**, 105 (1997).
37. J. W. Evans, Kinetic phase transition in catalytic reaction models, *Langmuir* **7**, 2514 (1991).
38. D. Horntrop, M. Katsoulakis, D. Vlachos, in preparation.
39. S. M. Allen and J. Cahn, A microscopic theory for antiphase boundary motion and its application to antiphase domain coarsening, *Acta. Metall.* **27**, 1089 (1979).
40. J. Fraaije, B. van Vlimmeren, N. Maurits, M. Postma, O. Evers, C. Hoffmann, P. Altevogt, and G. Goldbeck-Wood, The dynamic mean-field density functional method and its application to the mesoscopic dynamics of quenched block copolymer melts, *J. Chem. Phys.* **106**, 4260 (1997).
41. R. robert and J. Sommeria, Relaxation towards a statistical equilibrium state in two-dimensional perfect fluid dynamics, *Phys. Rev. Letters* **69**, 2776 (1992).
42. D. Kincaid and W. Cheney, *Numerical Analysis: Mathematics of Scientific Computing* (Brooks/Cole, Pacific Grove, GA, 1996).
43. N. Maurits, P. Altevogt, O. Evers, and J. Fraaije, Simple numerical quadrature rules for Gaussian chain polymer density functional calculations in 3D and implementation on parallel platforms, *Comp. Polym. Sci.* **6**, 1 (1996).
44. K. Morton and D. Mayers, *Numerical Solution of Partial Differenttial Equations* (Cambridge Univ. Press, Cambridge, UK, (1994).
45. J. Thomas, *Numerical Partial Differential Equations: Finite Difference Methods* (Springer-Verlag, Berlin/New York, 1995).
46. C. Canuto, M. Hussaini, A. Quarteroni, and T. Zang, *Spectral Methods in Fluid Dynamics* (Springer-Verlag, Berlin/New York, 1988).
47. D. Gottlieb and S. Orszag, *Numerical Analysis of Spectral Methods: Theory and Applications* (Soc. for Indus. & Appl. Math. Philadelphia, 1977).
48. I. Lifshitz and V. Slyozov, The kinetics of precipitation from supersaturated solid solutions, *J. Phys. Chem. Solids* **19**, 35 (1961).
49. R. Pego, Front migration in the nonlinear Cahn–Hilliard equation, *Proc. Roy. Soc. London Ser. A* **422**, 261 (1989).
50. A Chakrabarti, R. Toral, and J. Gunton, Late stage coarsening for off-critical quenches: Scaling functions and the growth law, *Phys. Rev. E* **47**, 3025 (1993).
51. T. Rogers, K. Elder, and R. Desai, Numerical study of the late stages of spinodal decomposition, *Phys. Rev. B* **37**, 9638 (1988).
52. C. Roland and R. Desai, Kinetics of quenched systems with long-range repulsive interactions, *Phys. Rev. B* **42**, 6658 (1990).
53. C. Sagui and R. Desai, Kinetics of phase separation in two-dimensional systems with competing interactions, *Phys. Rev. E* **49**, 2225, (1994).
54. C. Elliott and A. Stuart, The global dynamics of discrete semilinear parabolic equations, *SIAM J. Numer. Anal.* **30**, 1622 (1993).
55. K. Binder, Collective diffusion, nucleation, and spinodal decomposition in polymer mixtures, *J. Chem. Phys.* **79**, 6387 (1983).